AMERICAN
METEOROLOGICAL
SOCIETY

Journal of Atmospheric and Oceanic Technology

The DOI for this manuscript is doi: 10.1175/JTECH-D-16-0141.1

The final published version of this manuscript will replace the preliminary version at the above DOI once it is available.

If you would like to cite this EOR in a separate work, please use the following full citation:

Thurai, M., S. Manić, M. Schönhuber, V. Bringi, and B. Notaroš, 2017: Scattering calculations at C-band for asymmetric raindrops reconstructed from 2D video disdrometer measurements. J. Atmos. Oceanic Technol. doi:10.1175/JTECH-D-16-0141.1, in press.

Scattering calculations at C-band for asymmetric raindrops reconstructed from 2D video disdrometer measurements

Merhala Thurai†[1], Sanja Manić[1], Michael Schönhuber[2], V. N. Bringi[1], and Branislav M. Notaroš[1]

[1]Department of Electrical and Computer Engineering
Colorado State University, Fort Collins, Colorado, USA

[2]Joanneum Research, Graz, Austria

Submitted to: Journal of Atmospheric and Oceanic Technology,
November 2016

† Corresponding Author:
Merhala Thurai
Colorado State University
Department of Electrical and Computer Engineering
1373 Campus Delivery
Fort Collins, CO 80523, USA
Phone: (970) 491- 7678:
E-mail: merhala@engr.colostate.edu

ABSTRACT

The distribution of raindrop shapes is well-known to be important in deriving retrieval algorithms for drop size distribution parameters (such as the mass-weighted mean diameter) and rain rate, as well as for attenuation-correction using the differential propagation phase constraint. Whilst past work has shown that in the vast majority of rain events, the most 'probable' shapes conform to those arising primarily from the axisymmetric (2,0) oscillation mode, a more recent event analysis has shown that drop collisions can give rise to mixed mode oscillations and that for high collision rate scenarios, a significant percentage of drops can become 'asymmetric' at any given instant.

As a follow-up to such studies, we have performed scattering calculations for 3D-reconstructed shapes, of asymmetric drops using the shape measurements from a 2D video disdrometer (2DVD) during the abovementioned rain event. A recently developed technique is applied to facilitate the 3D reconstruction from the 2DVD camera data for these asymmetric drops. The reconstruction requires a specific technique to correct for the drop distortions due to horizontal velocities. Scattering calculations for the reconstructed asymmetric drops have been performed using a higher order method of moments solution to the electric and magnetic field surface integral equations. Results show that the C-band scattering amplitudes of asymmetric drops are markedly different from those of oblate spheroids. Our future intention is to automate the entire procedure so that more realistic simulations can be performed using the 2DVD-based data, particularly for cases where collision-induced drop oscillations give rise to considerable numbers of asymmetric drops.

1. Introduction

It is well known that drop size and shape (or axis ratio) distributions of raindrops are important factors in deriving retrieval algorithms for drop size distribution (DSD) parameters and rain rate (Seliga and Bringi 1976), as well as for attenuation-correction at higher frequencies (C- and X-bands) from polarimetric radar (e.g., Doviak and Zrnic 1993; Bringi and Chandrasekar 2001, and references contained therein). Previous work on drop shapes has ranged from laboratory and wind-tunnel measurements (see Beard et al. 2010 for a more recent review) to inferences from polarimetric data (Goddard et al. 1982, Gorgucci et al., 2006, Gourley et al. 2009), as well as theoretical modelling studies (for example, Beard and Chuang 1987). Additionally, the 2D-video disdrometer (2DVD) (Schönhuber et al. 2000 and 2008) has been utilized to determine drop shapes from an 'artificial rain' experiment (Thurai et al. 2007), as well as in natural rain (as reported in Beard et al. 2010, for example).

A thorough examination of the 2DVD camera data in natural rain from several locations have shown that in the vast majority of cases, the most 'probable' shapes conform to those arising primarily from the axisymmetric (2,0) oscillation mode (Beard et al. 2010). The other two oscillation modes, namely, mode (2,1) and mode (2,2), did not seem to be contributing significantly to the probable shapes. When (2,0) is the dominant oscillation mode, one would expect the drop shapes to be rotationally symmetric, whereas if the oscillation amplitudes of the other modes become significant then drop shapes will be expected to become asymmetric. For the latter case, the lack of symmetry can be detected from the image projections from the 2DVD camera data.

Such a scenario was found to be the case in a recent study (Thurai et al. 2013 and 2014a) using two collocated 2DVD instruments and the C-band polarimetric radar, ARMOR (Petersen et al. 2007; Crowe et al. 2012), in Huntsville, Alabama. The study showed that for this event (occurred on 25 Dec 2009), which had a highly organized line convection embedded within a larger rain system, significant fraction of the moderate-to-large sized drops did not possess rotational symmetry when the convection line passed over the 2DVDs. These inferences were made based on the ability (or not) to successfully 'deskew' the camera images of all the individual drops. More than 30% of the 3 mm and larger drops were found to be non-deskewable. Additionally ARMOR radar data analyses also showed that our most probable drop shape assumptions were not accurate nor applicable within the (rain-dominated) convection line. The lack of symmetry for such a large fraction of the drops was attributed to mixed-mode oscillations occurring within the intense rain shafts, which in turn were attributed to frequent, and sustained, drop collisions. The calculated collision rates were found to be highly correlated with the percentage of asymmetric drops. It is important to note here that if the collision rate becomes comparable to the decay time of the collision-induced drop oscillations, then sustained drop collisions can cause significant fraction of the drops at any instant in time to be in mixed mode oscillation state (and not have rotational axis of symmetry).

In this paper, we revisit the 25 Dec 2009 Huntsville event in order to reconstruct the shapes for raindrops which did not possess symmetry axis. In Section 2, we summarize the procedures needed to 3D reconstruct such asymmetric drops based on 2DVD measurements (Schönhuber et al., 2016; Schwinzerl et al., 2016), with an illustrative rain drop example from the Huntsville event. Section 3 presents an accurate, efficient, and versatile technique for electromagnetic scattering analysis of reconstructed drops, which includes surface integral equation (SIE) based modeling of drops and numerical solution using higher order method of moments (MoM) (Notaroš 2008; Chobanyan et al. 2015), as well as post-processing of MoM-SIE current-distribution coefficients to obtain polarimetric radar observables and MoM-SIE mesh generation from 2DVD-based 3D reconstructions of drops. In Section 4, we present example results of C-band scattering amplitudes and single drop differential reflectivity calculations for a number of asymmetric drops with different sizes whose realistic shapes are 3D-reconstructed from 2DVD measurements and accurately modeled by MoM-SIE surface meshes of quadrilateral patches, and compare them to those for rotationally symmetric drops. Other polarimetric radar parameters are also considered and evaluated. This is followed by Conclusions in Section 5.

2. 2DVD contours and reconstructing asymmetric drops in 3D

The 2DVD has two orthogonally placed light sources and two high speed line scan cameras giving rise to an intersection area of approximately 10 cm by 10 cm. The two light planes are vertically separated, and the separation, including any non-parallelism, is calibrated with high precision metallic spheres. The precise calibration enables the fall velocity of each particle to be determined accurately. Details of the instrument as well as the calibration procedures are given in Schönhuber et al. (2007, 2008).

2.1 2DVD contour data

The optical set-up allows the measurements of the drop contours in the two perpendicular planes, *viz.* x-z and y-z, where z represents the zenith. When a drop has a horizontal velocity component however, the measured contours will become distorted or skewed. Prior publications (Schönhuber 1998, Schönhuber et al. 2000, and later in Huang et al., 2008) have described in detail the procedures to deskew the contours of such drops which are skewed by their horizontal movement. However, the main assumption in the deskewing procedure for each drop is that it possesses an intrinsic axis of rotational symmetry. For such cases drops, the deskewing procedures will successfully output the corrected contours – which can then be used to derive the shape and the orientation – as well as the drop horizontal velocity in the x-y plane. (Appendix A1 shows these velocities compared with independent, collocated, wind sensor data). Note that the drop volume derived from the two deskewed contours will be the same as that from the two measured contours.

2.2 Deskewing procedure for drop horizontal velocity

For drops which do not have a well-defined axis of rotational symmetry (referred to as asymmetric drops hereafter), one or both of the measured contours will not meet the necessary criteria for the deskewing algorithm to be successful. Consider the example shown in Fig. 1, which shows a raindrop measured during the aforementioned 25 December 2009 event in Huntsville, Alabama. The equi-volume spherical diameter (D_{eq}) of the drop is 4.81 mm. The two measured contours in the x-z and the y-z planes are given in panels (a) and (b) respectively. In both cases, the straight lines connecting the middle of the top and the middle of the bottom scan lines are shown. Panel (c) shows the same contour as panel (b), but after the (successful) correction of the distortion caused by the drop horizontal velocity component in the y-z plane. The longest line which lies orthogonal to the axis of symmetry is highlighted by a relatively darker color. This can be considered as the ‘equator’ of the drop. The restoration of the orthogonality yields as a byproduct the horizontal velocity component in that plane. In the case of panel (b), this value was 5.85 m/s towards the left. Note that the recovered symmetry axis in panel (c) is not the necessarily same as the straight line in panel (b).

On the other hand, for the contour in panel (a), an axis of symmetry could not be established by the deskewing procedure and hence the drop horizontal velocity cannot be estimated in that plane. For such unusual cases, an alternative method has been very recently developed (Schönhuber et al., 2016; Schwinzerl et al., 2016). Details of the step-by-step procedure are given in Schönhuber et al. (2016), hence only the salient points are summarized here, and the aforementioned 4.81 mm drop is used specifically in this paper as an illustrative example.

2.3 Deskewing procedure for asymmetric drops

The main requirement is to first output, for a given plane, all known horizontal velocity components for all drops of similar size which do have symmetry axis. These velocity values are then interpolated in time to estimate the velocity component for the asymmetric drops. Fig. 2 shows the horizontal drop velocities of all drops with D_{eq} greater than 2 mm. The velocities are derived from the corresponding camera A contours, within a 'zoomed-in' time period of 7.2 seconds. The solid line represents these velocities. The vertical line shows the time of the drop corresponding to Fig. 2 for which the time interpolation is required The time interpolated velocity value so derived is then used for correcting the measured contour in Fig. 1(a) using the same procedure as in Schönhuber et al. (2016).

The corrected contour is shown in Fig. 3(a) as a thick red line. This panel also shows the contours corresponding to the preprocessing steps, starting from (i) the black dots which are the camera A's raw data, (ii) the green line which presents a linear interpolation based on the black dots, and (iii) its smoothed contour represented by the thin red line using an Akima algorithm (Gimpl 2012; also see Appendix of Thurai et al., 2007).

2.4 3D reconstruction

The next step is to generate a new set of points in each plane by resampling at various (and uniformly spaced) height intervals with typically 0.1 mm spacing. The center of gravity for each of the two contours is established, which are then shifted into the x = 0 and y = 0 plane respectively. Fig. 3(b) shows the two contours in x-y-z coordinate system.

Next, for each z = constant plane, each pair of neighboring points is used to derive a 90 deg segment of an ellipse. Examples for some of the z planes are over-plotted over each other in Fig. 3(c) which shows the corresponding ellipses in each quadrant with different colors. By stacking such sets of ellipses along the z-axis, it becomes possible to construct the drop shape in 3D. For the same drop we have considered thus far, the 3D reconstructed drop is shown in Fig. 4. Note, again, that the drop volume of the 3D reconstructed drop is the same as the drop volume originally determined from the raw data from the two cameras.

One possible limitation with respect to this 3D reconstruction is that it is limited by having only 2 orthogonal views rather than 3 (the third one being in the x-y plane). Given this restriction, one can only use the aforementioned 90 deg segment ellipses for the reconstruction. However, since rain drops (symmetric or otherwise) have relatively smooth surface and homogeneous (unlike snow particles which can have sharp discontinuities and are highly inhomogeneous), the errors in the 3D reconstructed shapes are not likely to be significant. Also to be noted is the relatively fine spacing for each slice, as can be gleaned from Fig. 3(c) which shows the slices in some, but not all, of the z-planes.

In the next section, we describe the method to calculate the forward and back scatter amplitudes using such 3D reconstructed raindrops as input.

3. Scattering analysis of reconstructed drops

3.1. Surface integral equation based electromagnetic modeling of asymmetric raindrops

Numerical modeling and analysis of electromagnetic scattering from asymmetric raindrops whose shapes are 3D-reconstructed based on 2DVD measurements is performed using a numerically rigorous full-wave computational electromagnetics approach invoking the method of moments (MoM) in the surface integral equation (SIE) theoretical formulation and a higher order numerical implementation (Chobanyan et al. 2015; Notaroš 2008). To outline the MoM-SIE scattering analysis methodology, consider a dielectric scatterer (raindrop) of an arbitrary (asymmetric) shape and complex dielectric constant (permittivity) $\varepsilon = \varepsilon_r\varepsilon_0$ (and permeability μ_0), where $\varepsilon_r = 72.5 - j22.43$ (water at 5.625 GHz), situated in free space (air) and excited by a time-harmonic electromagnetic field of complex field-intensities $\mathbf{E}^{\rm inc}$ and $\mathbf{H}^{\rm inc}$ and frequency f ($f = 5.625$ GHz, C band), as shown in Fig. 5.

According to the surface equivalence principle, the electric and magnetic fields both inside the scatterer (interior region) and in the surrounding air (external region) can be expressed in terms of equivalent electric and magnetic fictitious (artificial) surface currents, of densities $\mathbf{J}_{\rm s}$ and $\mathbf{M}_{\rm s}$, placed on the surface S of the scatterer (Chobanyan et al. 2015). The boundary conditions for the tangential components of the total (scattered plus incident) electric and magnetic field vectors on S give (Djordjević and Notaroš 2004)

$$[\mathbf{E}^{\rm scat}(\mathbf{J}_{\rm s},\mathbf{M}_{\rm s},\varepsilon_0)]_{\rm tang} + (\mathbf{E}^{\rm inc})_{\rm tang} = [\mathbf{E}^{\rm scat}(-\mathbf{J}_{\rm s},-\mathbf{M}_{\rm s},\varepsilon)]_{\rm tang}, \tag{1}$$

$$[\mathbf{H}^{\rm scat}(\mathbf{J}_{\rm s},\mathbf{M}_{\rm s},\varepsilon_0)]_{\rm tang} + (\mathbf{H}^{\rm inc})_{\rm tang} = [\mathbf{H}^{\rm scat}(-\mathbf{J}_{\rm s},-\mathbf{M}_{\rm s},\varepsilon)]_{\rm tang}, \tag{2}$$

where $\mathbf{E}^{\rm scat}$ is the scattered electric field (Fig. 5), calculated as

$$\mathbf{E}^{\mathrm{scat}}(\mathbf{J}_{\mathrm{s}},\mathbf{M}_{\mathrm{s}},\varepsilon)=-\mathrm{j}\omega\mu_0\int_S\left(\mathbf{J}_{\mathrm{s}}g+\frac{1}{k^2}\nabla_{\mathrm{s}}\cdot\mathbf{J}_{\mathrm{s}}\nabla g\right)\mathrm{d}S+\int_S\mathbf{M}_{\mathrm{s}}\times\nabla g\mathrm{d}S\ , \tag{3}$$

with g and k denoting Green's function and wave number for the unbounded medium, respectively, and similarly for the scattered magnetic field, $\mathbf{H}^{\mathrm{scat}}$. Scattered fields in each of the two regions (i.e., on the two sides of Eqs. (1) and (2)) are computed assuming that the remaining space is filled with the medium of that region. Having in mind the integral expressions for fields $\mathbf{E}^{\mathrm{scat}}$ (in Eq. (3)) and $\mathbf{H}^{\mathrm{scat}}$, Eqs. (1) and (2) represent a set of coupled electric/magnetic field surface integral equations (SIEs) for $\mathbf{J}_{\mathrm{s}}$ and $\mathbf{M}_{\mathrm{s}}$ as unknown quantities, which can be discretized and solved using the MoM.

3.2 Higher order MoM numerical solution of SIEs and evaluation of radar observables

In our higher order MoM-SIE technique, the surface S in Fig. 5 and Eq. (3) is modeled using generalized curved parametric quadrilaterals of arbitrary geometrical orders K_u and K_v (K_u, $K_v \geq 1$) and the current density vectors, $\mathbf{J}_{\mathrm{s}}$ and $\mathbf{M}_{\mathrm{s}}$, over quadrilaterals in the model are approximated by means of hierarchical-type vector basis functions of arbitrary current-expansion orders N_u and N_v (N_u, $N_v \geq 1$) (Djordjević and Notaroš 2004; Chobanyan et al. 2015). Note that even the quadrilateral of the first geometrical order, with $K_u = K_v = 1$, the so-called bilinear patch (Notaroš 2008) provides good flexibility for geometrical modeling; it is determined solely by four interpolation points – its four vertices, which can be arbitrarily positioned in space (do not need to be coplanar), and its edges and all coordinate lines are straight, while its surface is somewhat curved (inflexed).

The unknown coefficients in the expansion of the current-distribution are determined by solving the SIEs in Eqs. (1) and (2), employing Galerkin method (Djordjević and Notaroš 2004), which applies another surface integration of the SIEs with testing (weighting) functions equal to the basis functions. With this, the SIEs are discretized into a system of N linear algebraic equations with N unknowns, which is solved utilizing a direct solver, based on LU factorization. Once the unknown coefficients are found, the currents $\mathbf{J}_s$ and $\mathbf{M}_s$ over any generalized quadrilateral patch in the model surface are computed, and $\mathbf{E}^{scat}$ is evaluated using Eq. (3).

Computation of $\mathbf{E}^{scat}$ at far field points, for vertical and horizontal polarizations of the incident field $\mathbf{E}^{inc}$, enables the matrix of scattering amplitudes, S, to be found. The S matrix elements are then used to calculate polarimetric radar measurables (Bringi and Chandrasekar 2001). Note that reconstructed rain particle models are centered at the coordinate origin and are observed from the x-y (horizontal) plane (z = 0) in Fig. 5.

3.3 MoM-SIE mesh generation from 2DVD-based 3D reconstructions of drops

The MoM-SIE surface geometrical models of raindrops, in Fig. 5, namely, the meshes of quadrilateral patches accurately representing the realistic drop shape, are constructed using the points of the 3D reconstructions obtained from 2DVD measurements, as explained in Section 2. In what follows, for simplicity – we describe the mesh generation procedure on a MoM-SIE geometrical model constructed from the simplest Lagrange generalized quadrilaterals, bilinear patch elements; the generalization to the procedure leading to models with elements of higher orders K_u and K_v (K_u, $K_v \geq 2$) is straightforward. Fig. 6(a) shows the bilinear quadrilateral mesh of the particular 2DVD-based raindrop reconstruction in Fig. 4. Each patch is defined by the respective four points (quadrilateral vertices) from the 3D reconstruction, as illustrated in Fig. 6(b). These four points are chosen in two pairs of points; namely, for the first element in the surface model, one pair of points is selected from the lowest horizontal cutting plane (2D contour) of the reconstructed 3D contour, such that the two points have consecutive values of the azimuthal angle position (e.g., points 1 and 2 in Fig. 6(b)). Points for the second pair are then adopted from the next horizontal cutting plane (points 3 and 4 in Fig. 6(b)), with each of them having a corresponding point in the first pair – with the same azimuthal angle position. The second element in the model is then defined similarly but with one point from each pair being shared with the first element. The remaining two points are adopted to have the next value of the azimuthal angle position, while each new point is in the same cutting plane with one of the shared points. Further elements in the mesh, that are between the first and the last horizontal cutting plane, are constructed in a similar fashion, so that the mesh becomes connected (with no gaps between elements). The elements at the top (or bottom) of the model are constructed using only the points from the first (or last) cutting plane (all four points belong to the same horizontal 2D contour).

4. Results and discussion

Whereas for rotationally symmetric raindrops, one would expect parameters such as Z_{dr} to be independent of the 'look-angle' ϕ in the *x*-*y* horizontal plane, for asymmetric drops, it is only reasonable to expect Z_{dr} to vary with ϕ. However, as described in Section 2, the cross-section in the *x*-*y* plane is generated with a double-ellipse using only four points derived from the two camera-based contours for a given *z*. Although this procedure can be justified for raindrops – because of their relatively smooth surface, with no sharp discontinuities – the method would also result in scattering cross-sections showing relatively smooth and somewhat periodic variation with ϕ.

Fig 7 shows the C-band ($f = 5.625$ GHz; water complex permittivity $\varepsilon_r = 72.5 - j22.43$) co-polar back scatter amplitudes for the 4.81 mm drop described earlier as the illustrative example

(Figs. 4 and 6). The real and imaginary parts for the horizontal and vertical polarizations are presented separately. Horizontal incidence is considered where θ in Fig. 5 is set to 0 deg. All four quantities show ϕ dependence, but in terms of the magnitude, the real part of the horizontal back scatter amplitude dominates. It is this variation which has the highest effect on the Z_{dr} variation with ϕ. The minimum and maximum values of the calculated Z_{dr} were 2.98 and 3.63 dB, respectively[‡]. This range of values lies below the Z_{dr} calculated for the equivalent raindrop with an oblate spheroid shape, which amounts to 3.8 dB and is ϕ independent.

The Z_{dr} variations for two drops with similar D_{eq} values, D_{eq_1} = 3.08 mm and D_{eq_2} = 3.09 mm, are provided in Fig.8, which also shows the drop shapes. Visual inspection of the shapes clearly indicates that the former has the transverse (2,1) oscillation mode playing a more significant role, whilst the latter features the horizontal (2,2) mode as more significant. Nevertheless, it is very likely that in both cases mixed mode oscillations were taking place, as was discussed in earlier publications (Thurai et al. 2013 and 2014a). The event analysis showed that the percentage of drops undergoing mixed mode oscillations was correlated with the collision rates calculated based on the measured drop size distribution at ground level.

The Z_{dr} variations for the two drops in Fig. 8 are very clearly different. Compared with the Z_{dr} calculated for the equivalent oblate spheroid (shown as dashed line), the 3.08 mm drop has lower values and the 3.09 mm drop has higher values. For the former, Z_{dr} values range from 0.062 to 0.071 dB, and for the latter they range from 2.64 to 3.62 dB. Compared with 1.7 dB for the oblate spheroid, the drop with apparently more dominant transverse oscillation component shows considerably lower Z_{dr}, whereas the drop with more horizontal mode oscillation shows considerably higher values.

[‡] Sensitivity studies were conducted to examine the effect of inaccuracies in drop horizontal velocities on the reconstructed drop shapes and the final scattering calculations; they showed that the resulting uncertainties were much less than the ϕ dependence on Z_{dr}.

A total of eight drops were selected as illustrative examples, from the 25 Dec 2009 event in Huntsville, Alabama. The drops were selected randomly, and their D_{eq} ranged from 3 mm to 5.3 mm. All eight drops had shown a lack of rotational symmetry. A summary of the range of Z_{dr} values, i.e., the maximum and minimum values in the range $0 \leq \phi \leq 360°$, are plotted against their D_{eq} in Fig. 9, and compared with those calculated for the equivalent oblate spheroid. All eight cases deviate from the dashed curve (the oblate spheroid results), some showing markedly different values. Most of the cases lie below the dashed curve, which implies that transverse oscillation mode tends to be more prevalent than the horizontal mode, at least for the larger sized drops. This may not be the case for moderate nor smaller sized drops (which were present in abundance for this rain event). Note that the axisymmetric (2,0) mode will always be present and the other two modes will be superimposed onto it (Szakall et al. 2010).

The shape of raindrops is also expected to affect other polarimetric radar parameters, and our calculations indeed show this to be the case. Summaries (ranges for $0 \leq \phi \leq 360°$) of the two main parameters, specific differential phase, K_{dp}, factor and specific differential attenuation, A_{dp}, factor calculated for all eight drops are shown in Fig. 10(a) and 10(b), respectively, where the K_{dp} factor is defined as Real$\{S_{hh} - S_{vv}\}$ and the A_{dp} factor is given by Imag$\{S_{hh} - S_{vv}\}$, with S_{hh} and S_{vv} being the corresponding forward scattering amplitudes given in Eq. (5). As with the Z_{dr}, the asymmetric drops undergo different variation with D_{eq} compared with oblate spheroids (dash-dot lines), but the ratio A_{dp} factor/K_{dp} factor shows – in Fig. 10(c) – similar variations between asymmetric drops and oblate spheroids. This means that K_{dp}-based correction for differential attenuation is not critically dependent on the presence of asymmetric drops.

Asymmetric drops would also be expected to have different variation of Z_{dr} with the elevation angle,θ, when compared with oblate spheroids. For the latter, it has been shown in the past (Ryzhkov et al. 2005; Thurai et al. 2014b) that for Rayleigh scattering, and for an oblate raindrop, the differential reflectivity in linear units, z_{dr}, has the following θ-angle dependence:

$$z_{dr}(\theta) = \left| 1 + \left\{ \left(\frac{1}{\sqrt{z_{dr}(0)}} - 1 \right) \cos^2(\theta) \right\} \right|^{-2} \tag{4}$$

where $z_{dr}(0)$ is Z_{dr} in linear units for $\theta = 0°$.

In Fig. 11, we compare this theoretically-derived single-drop elevation dependence of Z_{dr}, shown as gray circles, with that calculated using the MoM-SIE technique for one of the eight asymmetric, reconstructed drops, shown as black plus marks. In both cases, the D_{eq} was 3.9 mm and calculations were done for C-band. For the oblate drop, the maximum Z_{dr} of 2.35 dB is reached at $\theta = 0°$ elevation, whereas for the asymmetric drop, the maximum Z_{dr} is 2.6 dB, which is slightly higher, and this is reached at $\theta = 10°$ elevation. Note also that the asymmetric drop shows negative Z_{dr} for the high elevation angles (although its magnitude is rather low), whereas the Z_{dr} of the oblate drop goes to zero – as expected – for $\theta = 90°$. The differences between the two cases are not only due to shape differences but also due to Rayleigh scattering assumption for the oblate spheroid case. For further comparisons, Fig. 11 also includes single particle T-matrix calculations for the same drops with the 'most probable shape'. As expected, these are close to eq. (4) than the MoM-SIE calculations.

Finally, we consider the cross-polar backscatter in terms of single particle LDR. Both LDR_{vh} and LDR_{hv} were considered, i.e., for 'h' transmit, 'v' receive and vice-versa. As with the Z_{dr} calculations, our LDR computations show, once again, ϕ angle variation. Table 1 shows the LDR values averaged over the full ϕ angle for three of the eight drops, along with their maximum and minimum values. The transmit 'h', receive 'v', as expected, shows lower LDR values. Also included are the Z_{dr} values for the three drops. In theory, the difference between LDR_{hv} and LDR_{vh} should correspond to Z_{dr}, and, as seen, this is indeed the case with our computations as well. Another point to note is that drops #261 and #492 have very similar D_{eq} but significantly different LDR values. These are the same two drops considered earlier in Fig. 8, and as mentioned earlier, the former (#261) seems to have (2,2) mode more dominant, whilst the transverse mode apparently dominates for the latter (#492). The latter produces higher LDR values.

Oblate drops with a typical Gaussian canting angle distribution with mean zero and standard deviation of 5° to 7.5° would be expected to give very low values of LDR (< −30 dB in most cases). By comparison, Table 1 shows significantly higher LDR values for the asymmetric drops. Hence if the fraction of large asymmetric drops is sufficiently high within the radar pulse volume, then LDR will be significantly enhanced, and detectable even with modest cross-polar performance C-band antenna. Higher than expected LDR values has been observed in previous studies, e.g., Jameson and Durden (1996) for Ku-band radar at nadir incidence, and has been ascribed as being due to high drop collision rates.

Significant fraction of asymmetric drops in the radar pulse volume will, by extrapolation, be expected to give rise to significantly different Z_{dr}, K_{dp}, and A_{dp} when compared with the oblate spheroid assumption (for a given DSD). The 2DVD is capable of providing the necessary information on the individual drop shapes (albeit at ground level) which can be used directly as input to the MoM-SIE method to calculate the forward and back scatter amplitudes, which in turn can be integrated to simulate the radar observables. Our illustrative examples have shown the feasibility of this technique, and our future intention is to automate this procedure so that such variations as Z–Z_{dr} and Z–K_{dp} can be examined for cases where collision-induced drop oscillations give rise to the presence of considerable numbers of asymmetric drops. The variations can be examined not just at C-band but also S, X, Ku, Ka and W bands.

5. Conclusions

Collision-induced drop oscillations can give rise to asymmetric drops when they undergo mixed-mode oscillations. Whilst for vast majority of the cases, the percentage of such asymmetric drops is not likely to be high, for high-collision rate cases, one would expect a significant fraction of the drops to become asymmetric at a given instant in time. Utilizing 2DVD data during such an event, it has been possible to reconstruct the shapes of these drops. In order to correct for drop horizontal velocities, a recently developed technique has been applied. The technique outputs all known horizontal velocities (from both 2DVD cameras) for drops of the same size that do have symmetry axis and for which the data processing algorithm can determine these velocities in the x-y plane, This set of values is then interpolated in time for the asymmetric drops. The velocity vectors so derived are then used for correcting the recorded contours in the x-z and the y-z planes for each individual drop, and the corrected contours are subsequently used to construct the corresponding 3D shapes.

The reconstructed drop shapes are then meshed and used as input to the MoM-SIE method to derive the forward and back scatter amplitudes at C-band. Our results for a selected number of drops have highlighted the following:

1. Z_{dr} shows a ϕ-angle dependence, but a quasi-periodic variation is observed because of the method of reconstruction; nevertheless, the ranges of values are distinctly different from those for equivalent oblate spheroids, which also are ϕ-independent. Moreover, two examples of drops with the same D_{eq} (= 3.1 mm) show different ϕ-variations, one

indicating the (2,1) oscillation mode being more dominant, and the other with the (2,2) mode dominating. As expected, the former shows considerably lower and the latter considerably higher Z_{dr} range when compared with the oblate spheroid shaped drop with the same D_{eq}.

2. The other two polarimetric parameters, which we have represented by A_{dp} factor and K_{dp} factor, also show ϕ-angle dependence, but interestingly, their ratios do not differ markedly from those for the oblate spheroids. This implies that K_{dp}-based correction for differential attenuation is not critically dependent on the presence of asymmetric drops.
3. Some differences in elevation dependence are also observed for the asymmetric drops when compared with theoretically-derived variation for the oblate spheroids, but these differences are not only due to shape differences but also due to Rayleigh scattering assumption for the oblate spheroid case.
4. Considerable differences in the range of LDR values are seen, and our results imply that if a significant fraction of the large drops within the radar pulse volume have asymmetric shapes, then LDR may be detectable even with modest cross-polar performance C-band antenna.

To derive the overall Z_h–Z_{dr}, Z_h–K_{dp} variations etc. needed for DSD retrievals and rainrate estimations, ideally one needs to take into account the shapes of each drop in *x*, *y*, *z* coordinates (or the equivalent *r*, θ, ϕ coordinates). Our 3D reconstruction of the drops using the *x-z* and *y-z* contours overcomes the need to have assumptions regarding drop canting angles. The output of the reconstruction procedure can be readily used as input to the MoM-SIE technique for scattering calculations, not just at C-band, but S-band, X-band, and higher frequency bands. Our future intention is to automate this procedure so that the aforementioned variations like Z–Z_{dr} and

Z–K_{dp} can be examined for cases where collision-induced drop oscillations give rise to the presence of considerable numbers of asymmetric drops.

Appendix A1

Drop horizontal velocities and wind sensor data

As mentioned in section 2 and as described in Schönhuber (1998), Schönhuber et al. (2000), and later in Huang et al., (2008) the deskewing procedures not only enable the drop contours to be corrected for horizontal movement for each drop but also output as a byproduct the horizontal velocity components from the front and the side views (A and B). Fig. A1(a) shows these velocities for both cameras (aligned N-S and E-W respectively) for all drops with $D_{eq} > 2$ mm. To highlight the accuracy of these outputs, we show in Fig. A1(b) and Fig. A1(c), the magnitude and the direction of the drop horizontal velocities derived from the two cameras (thick black lines) compared with measurements from a collocated (and independent) wind-sensor (shown in grey). Smoothing has been applied to the magnitude of horizontal wind speed in order to show more clearly the excellent agreement. Wind direction also shows very-well correlated variation. These comparisons highlight the accuracies of the 2DVD deskewing procedures. They also imply that one could use the wind sensor data (instantaneous) to deskew contours of particles with more complicated shapes such as snow dendrites, aggregates etc.

Acknowledgements

This work was supported by the National Science Foundation under grant AGS-1431127. We also wish to thank Martin Schwinzerl and Günter Lammer for useful discussions on the 3D reconstruction methodology.

References

Beard, K. V., and C. Chuang, 1987: A new model for the equilibrium shape of raindrops, *J. Atmos. Sci.*, **44**, 1509–1524.

Beard, K. V., V.N. Bringi, and M. Thurai, 2010: A new understanding of raindrop shape, *Atmospheric Research*, **97**, 393-632.

Bringi, V.N., and V. Chandrasekar, 2001: *Polarimetric Doppler Weather Radar: Principles and Applications*, Cambridge University Press, 636 pp.

Chobanyan, E., N. J. Šekeljić, A. B. Manić, M. M. Ilić, V. N. Bringi, and B. M. Notaroš, 2015: Efficient and Accurate Computational Electromagnetics Approach to Precipitation Particle Scattering Analysis Based on Higher-Order Method of Moments Integral Equation Modeling. *J. Atmos. Oceanic Technol.*, **32**, 1745–1758.

Crowe, C.C., C.J. Schultz, M.R. Kumjian, L.D. Carey, and W.A. Petersen, 2012: Use of dual-polarization signatures in diagnosing tornadic potential, *Electronic Journal of Operational Meteor.*, **13**, 57-78.

M. Djordjević and B. M. Notaroš, 2004: Double higher order method of moments for surface integral equation modeling of metallic and dielectric antennas and scatterers, *IEEE Transactions on Antennas and Propagation*, **52**, 2118-2129.

Doviak, R. J., and Zrnić, D. S., 1993: *Doppler Radar and Weather Observations*, Second Edition, Academic Press, 562 pp.

Gatlin, P. N., M. Thurai, V. N. Bringi, W. Petersen, D. Wolff, A. Tokay, L. Carey, and M. Wingo, 2015, Searching for Large Raindrops: A Global Summary of Two-Dimensional Video Disdrometer Observations, *Journal of Applied Meteorology and Climatology*, **54**, 1069–1089.

Gimpl H., 2012: Optimised Algorithms for 2D-Video-Distrometer Data Analysis and Interpretation, Diploma thesis, Institute of Communication Networks and Satellite Communications, Graz University of Technology, Graz/Austria, 111 pp, supervised by W. L. Randeu and M. Schönhuber.

Goddard, J. W. F., S. M. Cherry, and V. N. Bringi, 1982: Comparison of dual-polarization radar measurements of rain with ground-based disdrometer measurements. *J. Appl. Meteor.*, **21**, 252–256.

Gorgucci, E., L. Baldini, and V. Chandrasekar, 2006: What Is the Shape of a Raindrop? An Answer from Radar Measurements, *J. Atmos. Sci.*, **63**, 3033–3044.

Gourley, J. J., A. J. Illingworth, P. Tabary, 2009: Absolute Calibration of Radar Reflectivity Using Redundancy of the Polarization Observations and Implied Constraints on Drop Shapes. *J. Atmos. Oceanic Technol.*, **26**, 689–703.

Huang, G-J, V. N. Bringi, and M. Thurai, 2008: Orientation Angle Distributions of Drops after an 80-m Fall Using a 2D Video Disdrometer, *J. Atmos. Oceanic Technol.*, **25**, 1717–1723.

Jameson, A. R., and S. L. Durden, 1996: A possible origin of linear depolarization observed at vertical incidence in rain, *J. Appl. Meteor.*, **35**, 271–277.

Notaroš, B. M., 2008: Higher order frequency-domain computational electromagnetics, Invited review paper, Special Issue on Large and Multiscale Computational Electromagnetics, *IEEE Trans. Antennas Propag.*, **56**, 2251−2276.

Petersen, W. A., K. R. Knupp, D. J. Cecil, and J. R. Mecikalski, 2007: The University of Alabama Huntsville THOR Center instrumentation: Research and operational collaboration, *Preprints, 33rd Int. AMS Conf. on Radar Meteorology*, Cairns, Australia. [Available online at https://ams.confex.com/ams/33Radar/webprogram/Paper123410.html.]

Ryzhkov, A. V., S. E. Giangrande, V. M. Melnikov, and T. J. Schuur, 2005: Calibration issues of dual-polarization radar measurements. *J. Atmos. Oceanic Technol.*, **22**, 1138–1155.

Schönhuber M., 1998: About Interaction of Precipitation and Electromagnetic Waves, Doctoral thesis, Institute of Communications and Wave Propagation, Technical University Graz, Austria, 181 pp, supervised by W. L. Randeu.

Schönhuber, M., H. Urban, J. P. V. Poires Baptista, W. L. Randeu, and W. Reidler, 1997: Weather radar versus 2D-video-distrometer data, *Weather Radar Technology for Water Resources Management*, B. Braga Jr. and O. Massambani, Eds., UNESCO Press, 159 – 171.

Schönhuber M., Lammer G., Randeu W.L., 2007: One decade of imaging precipitation measurements by 2D-video disdrometer, *Advances in Geosciences*, **10**, 85-90.

Schönhuber, M., G. Lammer, and W. L. Randeu, 2008: The 2D video disdrometer. *Precipitation: Advances in Measurement, Estimation and Prediction,* S. Michaelides, Ed., Springer, 3–31.

Schönhuber, M., M. Schwinzerl and G. Lammer, 2016: 3D Reconstruction of 2DVD-measured Raindrops for Precise Prediction of Propagation Parameters, *10th European Conference on Antennas and Propagation (EuCAP)*, Davos, 2016, pp. 1-4, doi: 10.1109/EuCAP.2016.7481929

Schwinzerl, M., Schönhuber, M., Lammer, G., and Thurai, M., 2016: 3D reconstruction of individual raindrops from precise ground-based precipitation measurements, *European Meteorological Society, EMS Annual Meeting Abstracts,* **13**, EMS2016-601, http://meetingorganizer.copernicus.org/EMS2016/EMS2016-601.pdf

Seliga, T.A. and V. N. Bringi, 1976: Potential Use of Radar Differential Reflectivity Measurements at Orthogonal Polarizations for Measuring Precipitation, *J. of Applied Meteorology*, **51**, 69-76.

Szakáll, M., K. Diehl, S. K. Mitra, and S. Borrmann, 2010: Shapes and oscillations of falling raindrops—A review. *Atmos. Res.*, **97**, 416−425.

Thurai, M., G. J. Huang, V. N. Bringi, W. L. Randeu, M. Schönhuber, 2007: Drop shapes, model comparisons, and calculations of polarimetric radar parameters in rain. *J. Atmos. Oceanic Technol.*, **24**, 1019−1032.

Thurai, M., V. N. Bringi, W. A. Petersen, P. N. Gatlin, 2013: Drop shapes and fall speeds in rain: two contrasting examples. *J. Appl. Meteor. Climatol.*, **52**, 2567−2581.

Thurai, M., V. N. Bringi, A. B. Manic, N. J. Sekeljic, and B. M. Notaros, 2014a: Investigating rain drop shapes, oscillation modes, and implications for radiowave propagation, *Radio Science*, **49**, 921-932.

Thurai, M., P. T. May, and A. Protat, 2014b: Shipborne Polarimetric Weather Radar: Impact of Ship Movement on Polarimetric Variables at C Band, *J. Atmos. Oceanic Technol.*, **31**, 1557–1563.

List of Figures

Figure 1: Raw data from (a) camera A, and (b) camera B of a recorded raindrop with D_{eq} = 4.81 mm from the 25 Dec 2009 Huntsville event; (c) the same side view as (b) but after correcting for distortion for drop horizontal velocity component in that plane, and after identifying the symmetry axis.

Figure 2: Drop horizontal velocity component of drops with D_{eq} > 2 mm from camera A data (east-to-west) obtained from measured contours where the axis of symmetry could be established (black line joining the diamond points). The vertical dashed line shows the time of the asymmetric drop contours in Fig.1(a).

Figure 3: Correction procedure for drop distortion due to horizontal motion for the drop in Fig. (1): (a) camera A's raw data (black dots), linear interpolation (green line), and smoothed contour using an Akima algorithm (thin red line), and the resulting corrected contour, using the velocity obtained from the time series interpolation (thick red line); (b) After aligning both contours together; (c) the four ellipse contours derived for a z = constant plane

Figure 4: Final full 3D reconstruction of the drop based on the procedure in Figs. 1, 2, and 3.

Figure 5: Surface integral equation (SIE) based electromagnetic scattering analysis of asymmetric raindrops modeled by method of moments (MoM) patches.

Figure 6: (a) MoM-SIE surface geometrical model (mesh) of the reconstructed asymmetric raindrop in Fig. 5 (raindrop #4530) generated using bilinear quadrilateral patches, in Fig. 7(b). (b) Mesh detail showing an element defined by four nodes (patch vertices).

Figure 7: MoM-SIE calculated ϕ angle variation of the real and imaginary parts of C-band (f = 5.625 GHz) back-scatter amplitudes for the 4.81 mm raindrop from Figs. 4 and 7, for the horizontal and vertical polarizations. (Note for S_{hh}, real and imaginary, the forward scattering alignment (FSA) convention is used). These scattering calculations have also been verified with other methods such as low-order HFSS code (industry standard utilizing the finite element method).

Figure 8: Z_{dr} variation with angle ϕ, computed by the MoM-SIE at C-band, for two drops with $D_{eq} \approx 3.1$ mm reconstructed using data from 2DVD-SN16 during the line convection event on 25 Dec 2009, Huntsville, Alabama. Shown also are the 3D-reconstructed shapes of the two drops, as well as the Z_{dr} of the equivalent oblate spheroid.

Figure 9: Range of Z_{dr} values (maximum and minimum Z_{dr} in the range $0 \le \phi \le 360°$) calculated, by the MoM-SIE, at f = 5.625 GHz for eight randomly selected asymmetric 3D-reconstructed drops (from the 25 Dec 2009 Huntsville event), against the respective D_{eq} values; comparison with the corresponding Z_{dr} values for equivalent oblate spheroids with the same D_{eq} (dashed line).

Figure 10: (a) K_{dp}_factor, (b) A_{dp}_factor, and (c) their ratio, in terms of D_{eq}, calculated (using the MoM-SIE) at C-band for the same eight drops as in Fig. 11, and compared with the results for oblate spheroids (dash-dot lines and square dots).

Figure 11: Elevation angle (θ) dependence of Zdr for a Deq = 3.9 mm drop (f = 5.625 GHz): comparison of the MoM-SIE computed results for the 3D-reconstructed 2DVD-measured shape with those obtained from the theoretically-derived Eq. (64). Also shown are the T-matrix calculations assuming the most probable drop shapes from Thurai et al., (2007).

Fig. A1: (a) Horizontal velocities for all drops with $D_{eq} > 2$ mm from cameras A shown as black points and B as grey points respectively; (b) Magnitude of the drop velocities determined from (a) shown as black points and wind speed from a collocated wind-sensor shown as grey points, both smoothed; (c) same as (b), but for direction, and with no smoothing.

List of Tables

Table 1: MoM-SIE computed C-band LDR averaged for $0 \leq \phi \leq 360°$ and maximum and minimum LDR values for three of the eight asymmetric drops from Fig. 11; averaged Z_{dr} values are also shown.

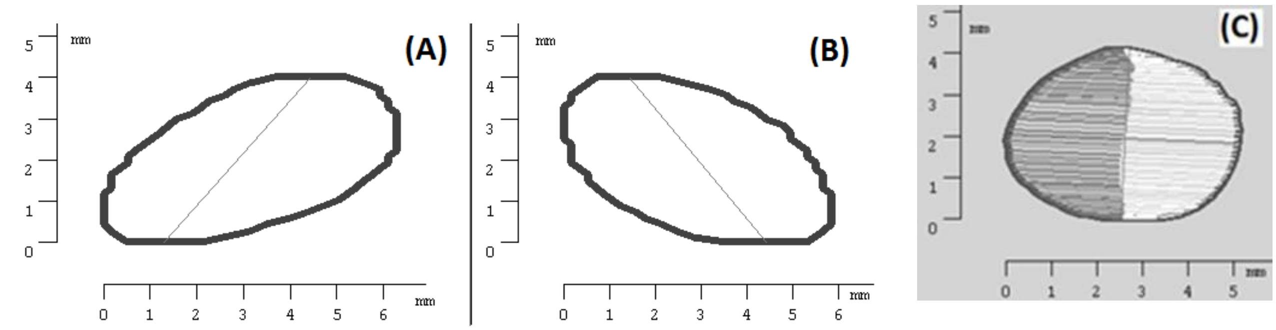

Figure 1: Raw data from (a) camera A (in the x-z plane), and (b) camera B (in the y-z plane) of a recorded raindrop with D_{eq} = 4.81 mm from the 25 Dec 2009 Huntsville event; (c) the same side view as (b) but after correcting for distortion for drop horizontal velocity component in that plane, and after identifying the symmetry axis.

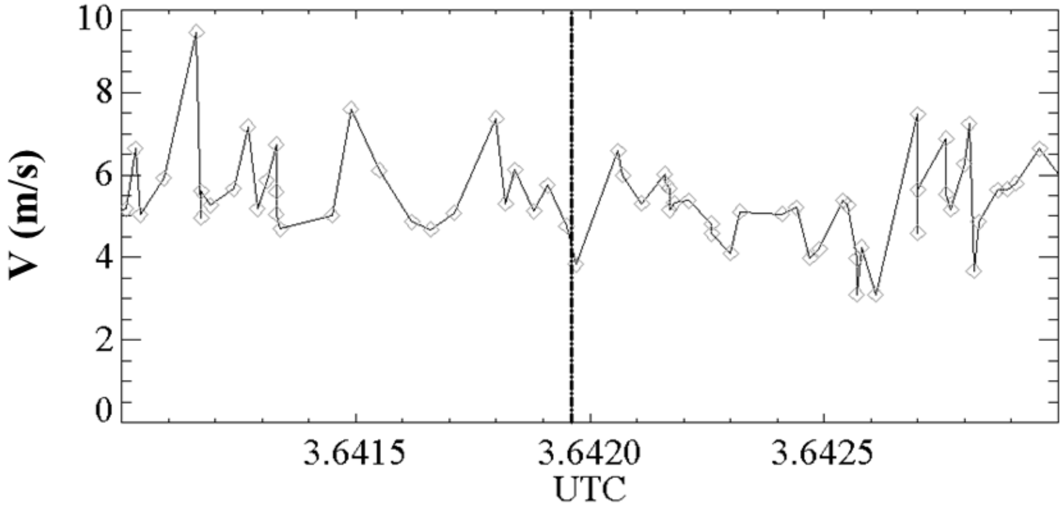

Figure 2: Drop horizontal velocity component of drops with D_{eq} > 2 mm from camera A data (east-to-west) obtained from measured contours where the axis of symmetry could be established (black line joining the diamond points). The vertical dashed line shows the time of the asymmetric drop contours in Fig.1(a).

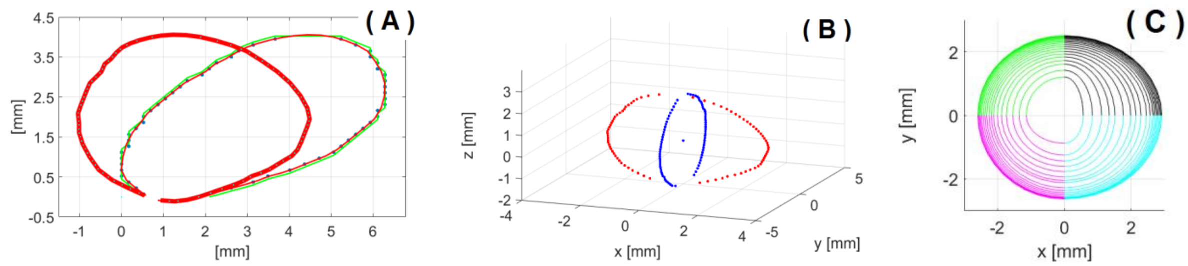

Figure 3: Correction procedure for drop distortion due to horizontal motion for the drop in Fig. (1): (a) camera A's raw data (black dots), linear interpolation (green line), and smoothed contour using an Akima algorithm (thin red line), and the resulting corrected contour, using the velocity obtained from the time series interpolation (thick red line); (b) After aligning both contours together; (c) the four ellipse contours derived for a z = constant plane.

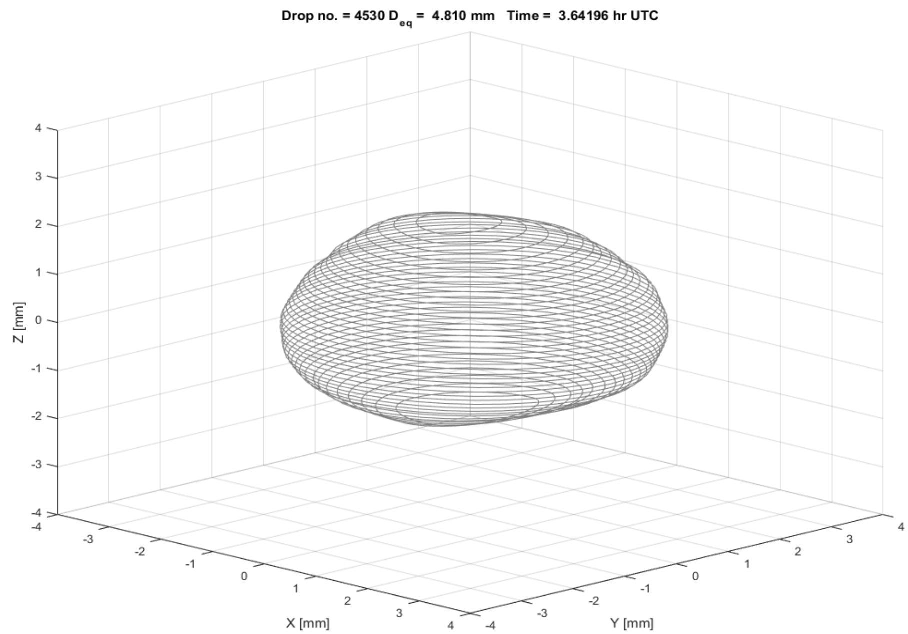

Figure 4: Final full 3D reconstruction of the drop based on the procedure in Figs. 1, 2, and 3.

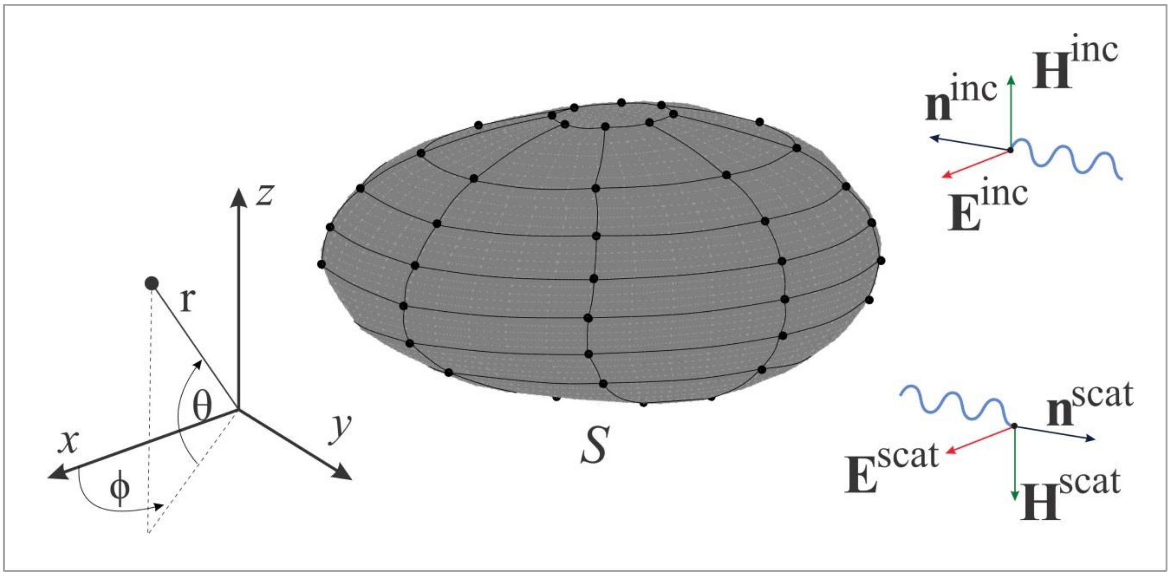

Figure 5: Surface integral equation (SIE) based electromagnetic scattering analysis of asymmetric raindrops modeled by method of moments (MoM) patches.

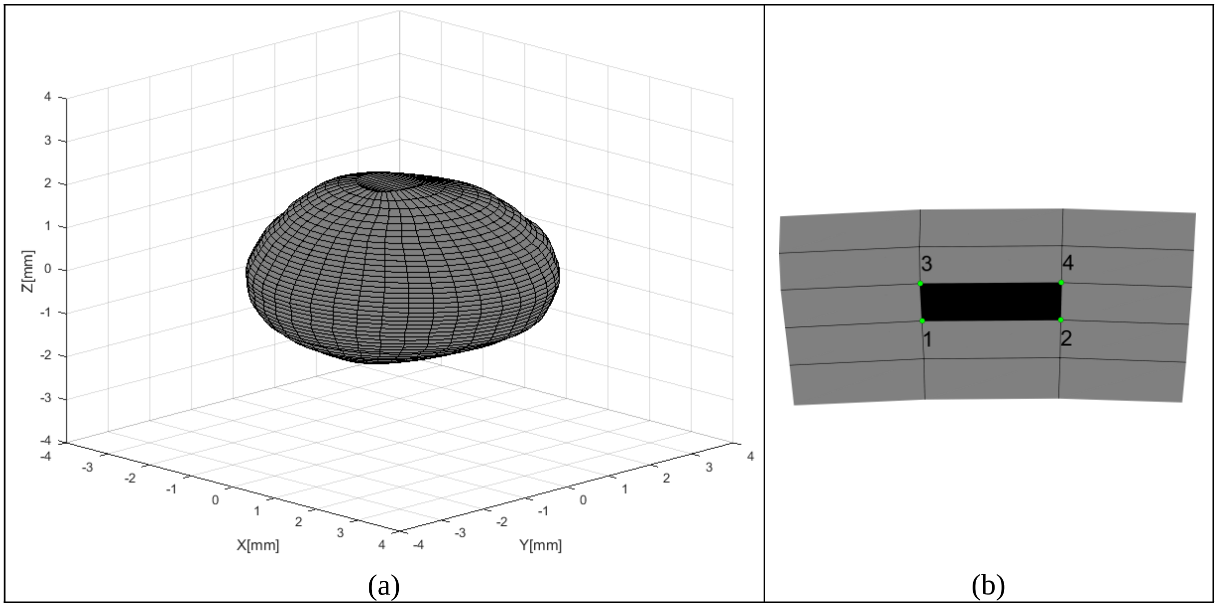

Figure 6: (a) MoM-SIE surface geometrical model (mesh) of the reconstructed asymmetric raindrop in Fig. 4 (raindrop #4530) generated using bilinear quadrilateral patches. (b) Mesh detail showing an element defined by four nodes (patch vertices).

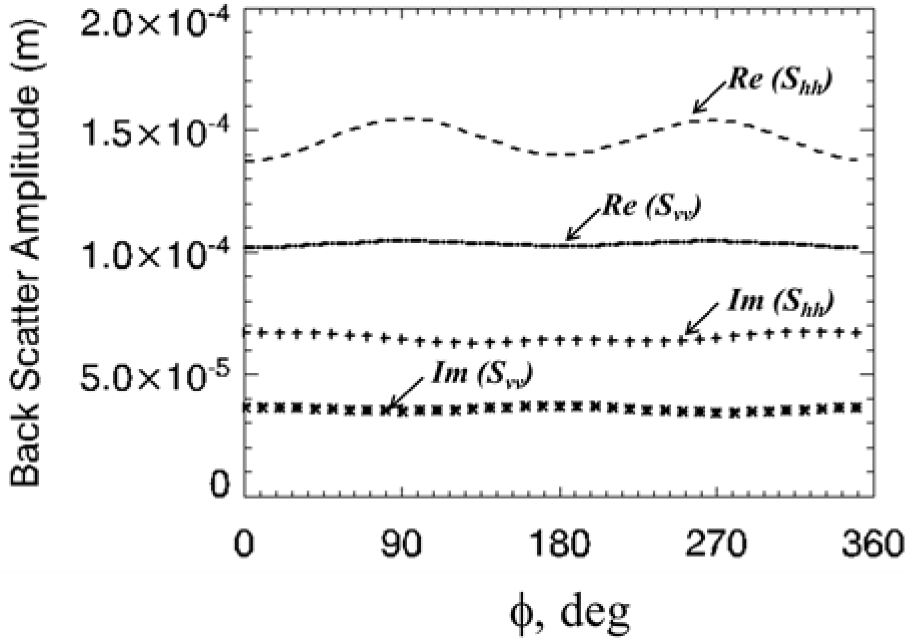

Figure 7: MoM-SIE calculated ϕ angle variation of the real and imaginary parts of C-band (*f* = 5.625 GHz) back-scatter amplitudes for the 4.81 mm raindrop from Figs. 4 and 6, for the horizontal and vertical polarizations. (Note for S_{hh}, real and imaginary, the forward scattering alignment (FSA) convention is used). These scattering calculations have also been verified with other methods such as low-order HFSS code (industry standard utilizing the finite element method).

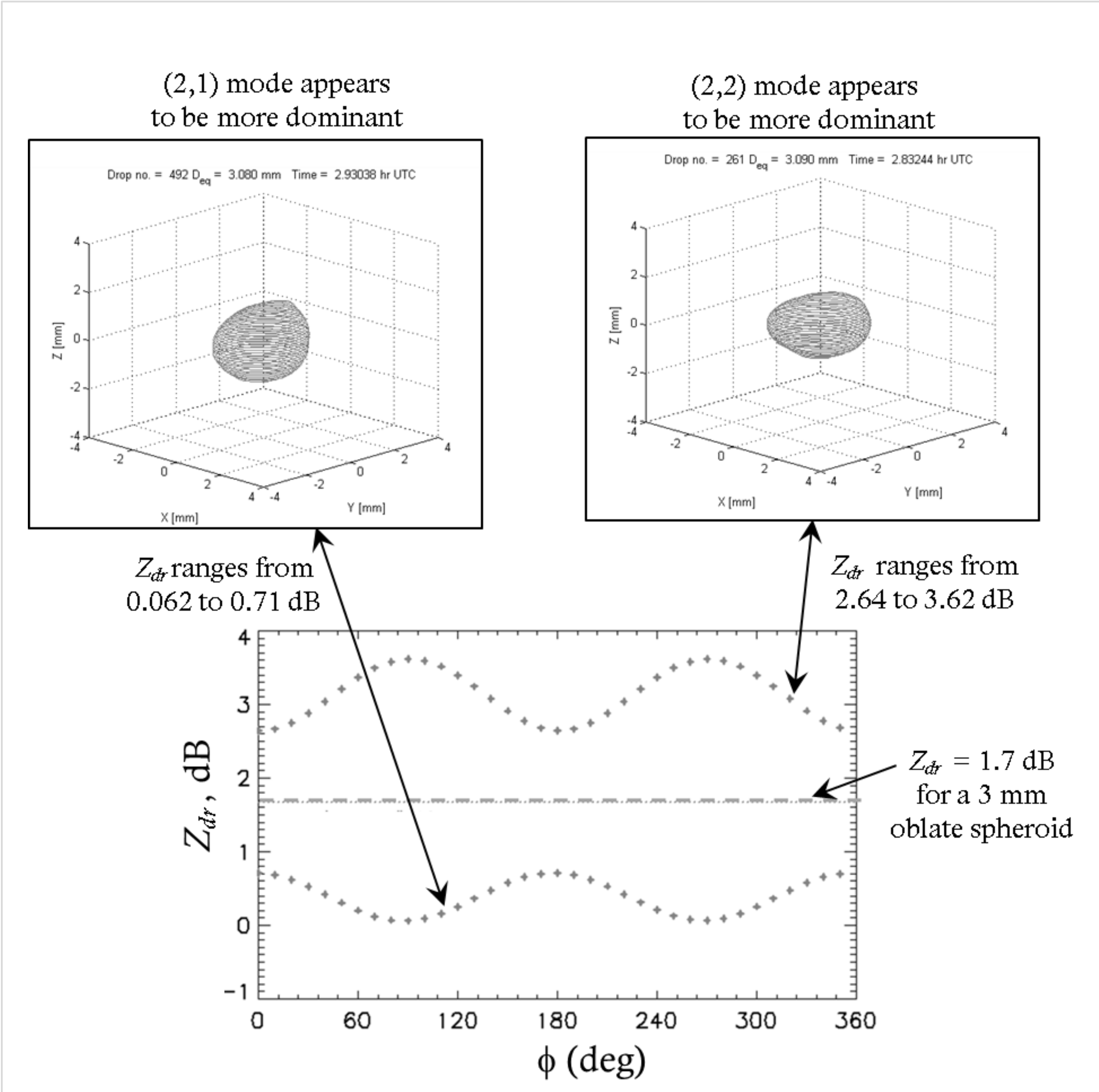

Figure 8: Z_{dr} variation with angle ϕ, computed by the MoM-SIE at C-band, for two drops with $D_{eq} \approx 3.1$ mm reconstructed using data from 2DVD-SN16 during the line convection event on 25 Dec 2009, Huntsville, Alabama. Shown also are the 3D-reconstructed shapes of the two drops, as well as the Z_{dr} of the equivalent oblate spheroid.

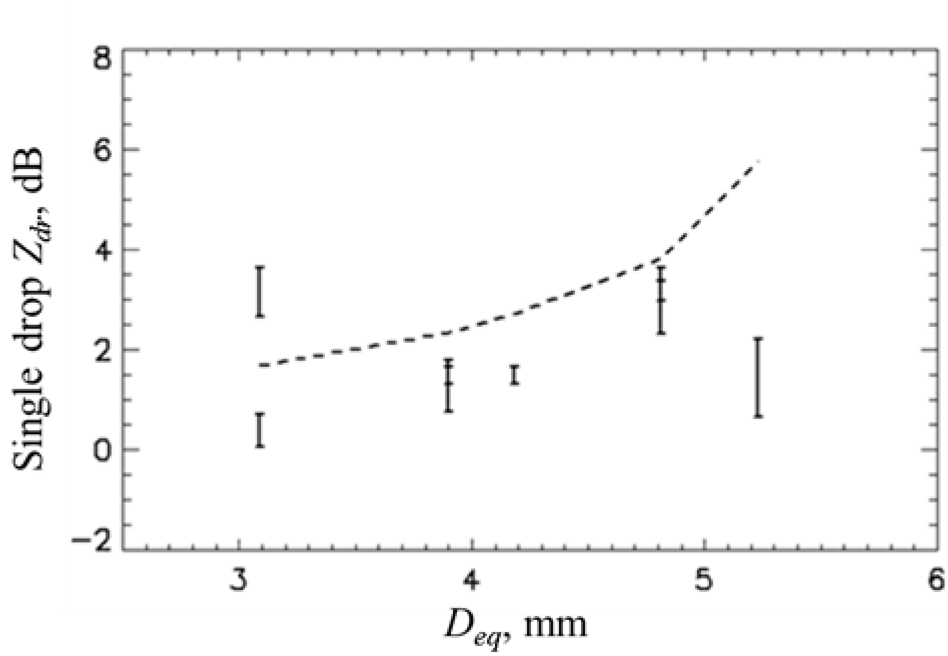

Figure 9: Range of Z_{dr} values (maximum and minimum Z_{dr} in the range $0 \leq \phi \leq 360°$) calculated, by the MoM-SIE, at f = 5.625 GHz for eight randomly selected asymmetric 3D-reconstructed drops (from the 25 Dec 2009 Huntsville event), against the respective D_{eq} values; comparison with the corresponding Z_{dr} values for equivalent oblate spheroids with the same D_{eq} (dashed line).

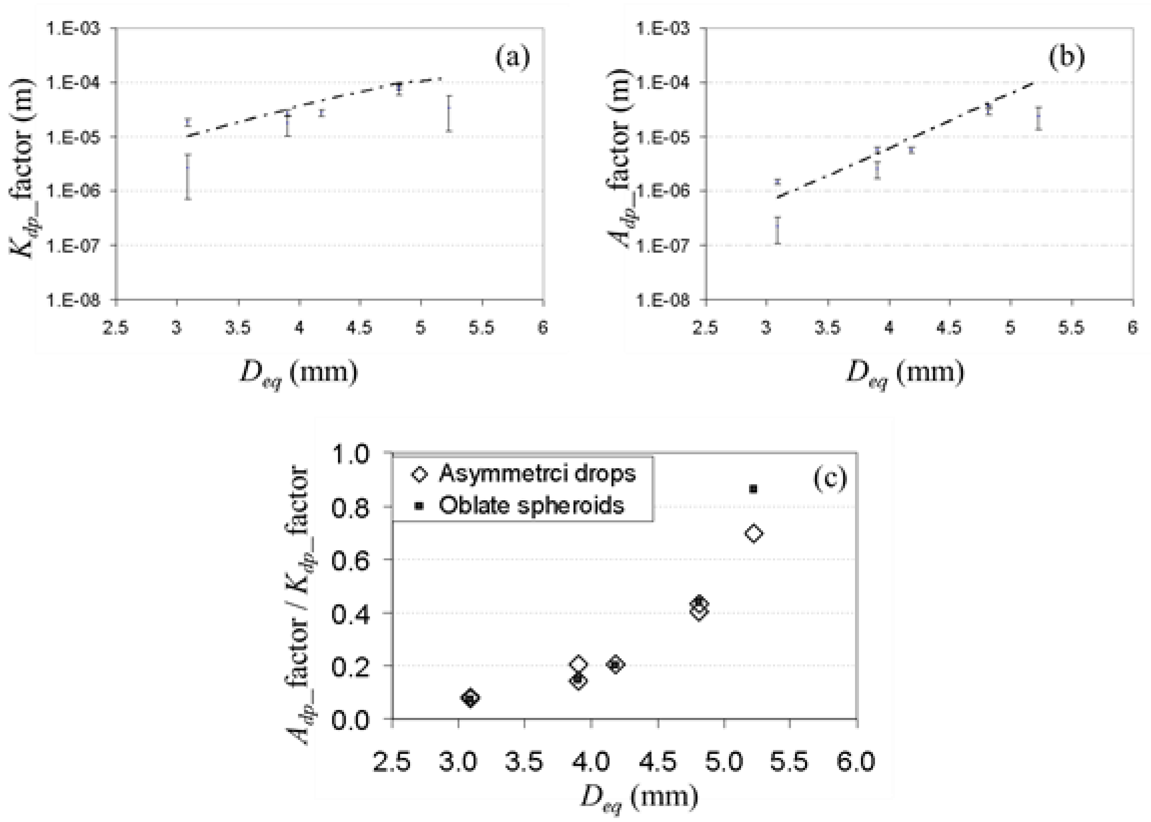

Figure 10: (a) K_{dp}_factor, (b) A_{dp}_factor, and (c) their ratio, in terms of D_{eq}, calculated (using the MoM-SIE) at C-band for the same eight drops as in Fig. 11, and compared with the results for oblate spheroids (dash-dot lines and square dots).

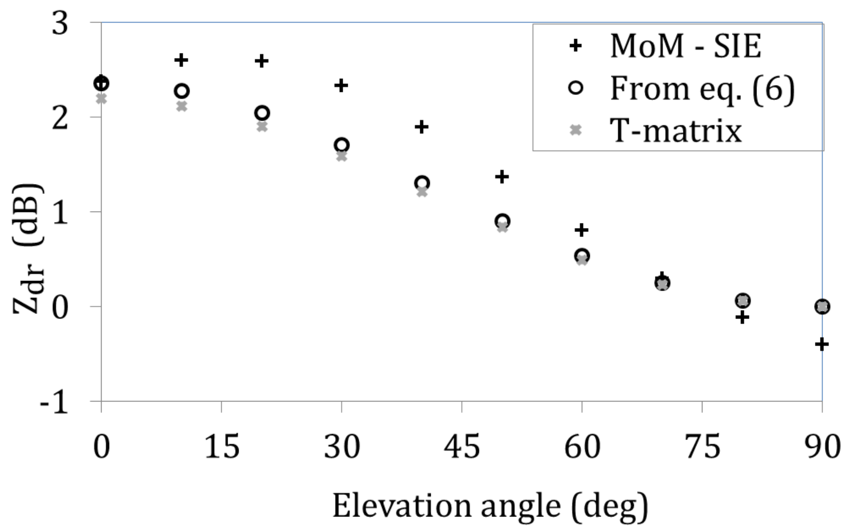

Figure 11: Elevation angle (θ) dependence of Z_{dr} for a D_{eq} = 3.9 mm drop (f = 5.625 GHz): comparison of the MoM-SIE computed results for the 3D-reconstructed 2DVD-measured shape with those obtained from the theoretically-derived Eq. (4). Also shown are the T-matrix calculations assuming the most probable drop shapes from Thurai et al., (2007).

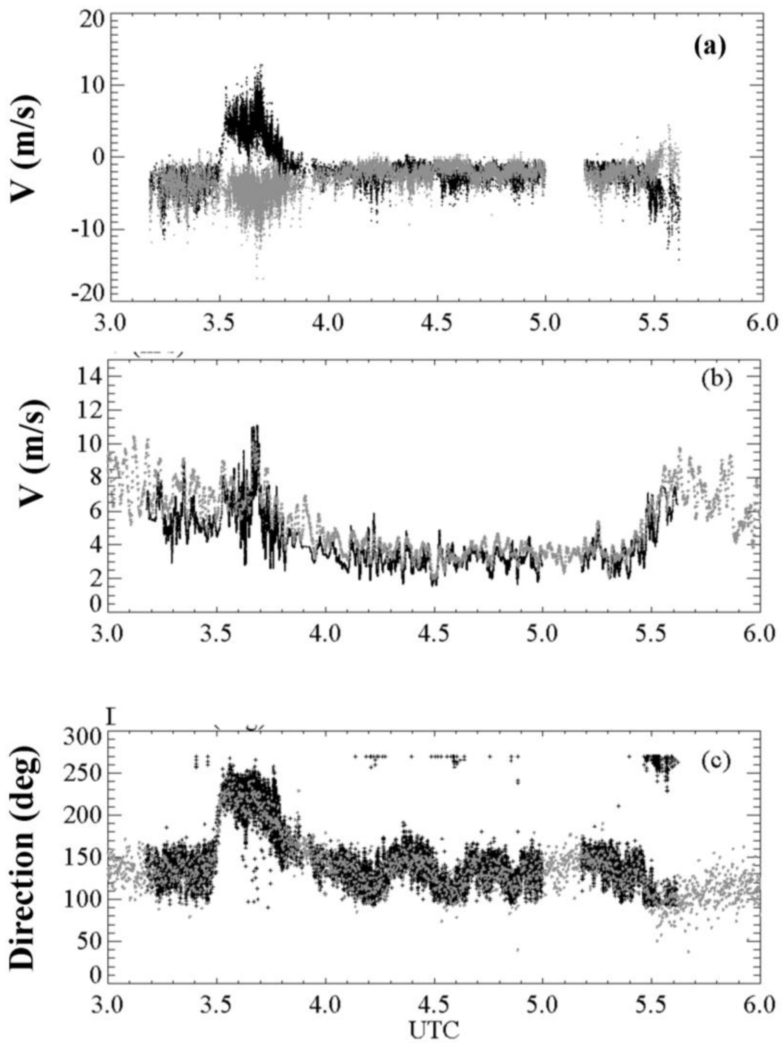

Fig. A1: (a) Horizontal velocities for all drops with D_{eq} > 2 mm from cameras A shown as black points and B as grey points respectively; (b) Magnitude of the drop velocities determined from (a) shown as black points and wind speed from a collocated wind-sensor shown as grey points, both smoothed; (c) same as (b), but for direction, and with no smoothing.

Table 1

MoM-SIE computed C-band LDR averaged for $0 \le \phi \le 360°$ and maximum and minimum LDR values for three of the eight asymmetric drops from Fig. 11; averaged Z_{dr} values are also shown.

Drop number	D_{eq}	Z_{dr} averaged over ϕ	LDR_{hv} averaged over ϕ (range of values)	LDR_{vh} averaged over ϕ (range of values)
#261	3.09 mm	3.15 dB	−26.7 dB (−24.1 to −49 dB)	−23.5 dB (−20.6 to −47 dB)
#492	3.08 mm	0.40 dB	−23.4 dB (−20.7 to −67 dB)	−23.0 dB (−17.8 to −65 dB)
#1416	4.18 mm	1.49 dB	−23.2 dB (−20. − to −51 dB)	−21.7 dB (−18.6 to −49 dB)